Structural design and analysis of an anisotropic, bi-axially morphing skin concept

Journal Article

Author(s):
Kölbl, Michael; Ermanni, Paolo

Publication date:
2022-01

Permanent link:
https://doi.org/https://doi.org/10.3929/ethz-b-000522583

Originally published in:
Aerospace Science and Technology 120, https://doi.org/10.1016/j.ast.2021.107292

Funding acknowledgement:
- Variable Stiffness Composite Metamaterials ()
- Optical measurement of three-dimensional surface displacement fields of morphing structures ()

Aerospace Science and Technology 120 (2022) 107292

Contents lists available at ScienceDirect

Aerospace Science and Technology

www.elsevier.com/locate/aescte

Structural design and analysis of an anisotropic, bi-axially morphing skin concept

Michael Kölbl *, Paolo Ermanni

ETH Zürich, Department of Mechanical and Process Engineering, Laboratory of Composite Materials and Adaptive Structures, Tannenstrasse 3, 8092 Zürich, Switzerland

ARTICLE INFO

Article history:
Received 27 May 2021
Received in revised form 8 November 2021
Accepted 15 December 2021
Available online 17 December 2021
Communicated by Grigorios Dimitriadis

Keywords:
Morphing skin
Adaptive structures
Morphing wing
Shape adaptation

ABSTRACT

Morphing skins as structural component in shape adaptive wings are still in their early development phase, as they need to combine contradicting requirements, such as extreme anisotropic mechanical behaviour, low structural thickness and air-tightness. Various morphing skin approaches have been designed for confined problems such as camber morphing and low load scenarios. However, to expand the applicability of morphing wings, a morphing skin with full in-plane deformability and an out-of-plane stiffness suitable for manned aircraft is necessary. In this work, a novel, elastomer free layered morphing skin is designed, manufactured, applied to a camber morphing transition region for small aircraft and analysed. The layered morphing skin is based on stacked, stiff platelets contributing to the out-of-plane stiffness, while compliant ligaments connecting the platelets provide in-plane compliance. Therefore, the layered morphing skin shows extreme orthotropy and can independently deform in both in-plane directions with an initial modulus of 198 kPa. Deformation analysis of the layered morphing skin on the camber morphing transition region confirms the bi-axial deformability and shows strains in span and chord up to 10% and 16%, respectively. Conducted pressure tests indicate an out-of-plane stiffness high enough for small aircraft, despite the demonstrator being manufactured from a polymer. The layered morphing skin concept is a promising base for bi-directionally deformable morphing skins.

1. Introduction

Used for the Wright Flyer in the early 20th century, morphing faded into the background due to the advances made in fixed wing and control surface design and the increasing size of aircraft. Over the last two decades morphing wings have gained broad engineering research interest again, as they promise higher efficiency across a wide range of flight conditions [1]. Although the benefits of morphing wings were shown for fuel burn [2], aerodynamics of control surfaces [3] and energy output for airborne wind energy systems [4], they have not been applied widely due the lack of suitable adaptive skins.

The morphing skin, as an indispensable part of the adaptive system [5,6], needs to combine mechanical, geometric and aerodynamic characteristics which directly contradict each other. The ideal morphing skin is thin, exhibits minimal in-plane stiffness in direction of actuation to achieve low actuation forces, but high out-of-plane stiffness to withstand aerodynamic loads [7–9]. It possesses a tailorable shear stiffness [3,8,10] and is drapeable for adapting to the morphed wing shapes. Its mass should be comparable to conventional skins with the surface being closed (free of holes) and smooth to avoid a drag penalty. From this set of properties, it is inevitable that a morphing skin must compromise and its applications are restricted: either to uni-axial strains in the case of camber morphing where anisotropic corrugated sheets with aerodynamic losses are used [11–15], to discrete morphing states [16], or to small geometric regions [17], where the skin's mass is of minor importance. Structurally efficient lattice structures compromise less on mechanical properties [18–23], but do not possess an aerodynamic surface by design and can therefore only act as structural support for the aerodynamic cover. The additional cover is often made from elastomers, exhibiting local buckling when subjected to aerodynamic loads and susceptibility to creep [10], limiting the application to low load scenarios [24].

The development of an ideal morphing skin would eventually boost the realisation of general multi-shape morphing wings with optimal aerodynamic efficiency [25]. However, recalling the contradicting morphing skin requirements and the difficulty to scale

* Corresponding author.
E-mail address: mkoelbl@ethz.ch (M. Kölbl).

https://doi.org/10.1016/j.ast.2021.107292

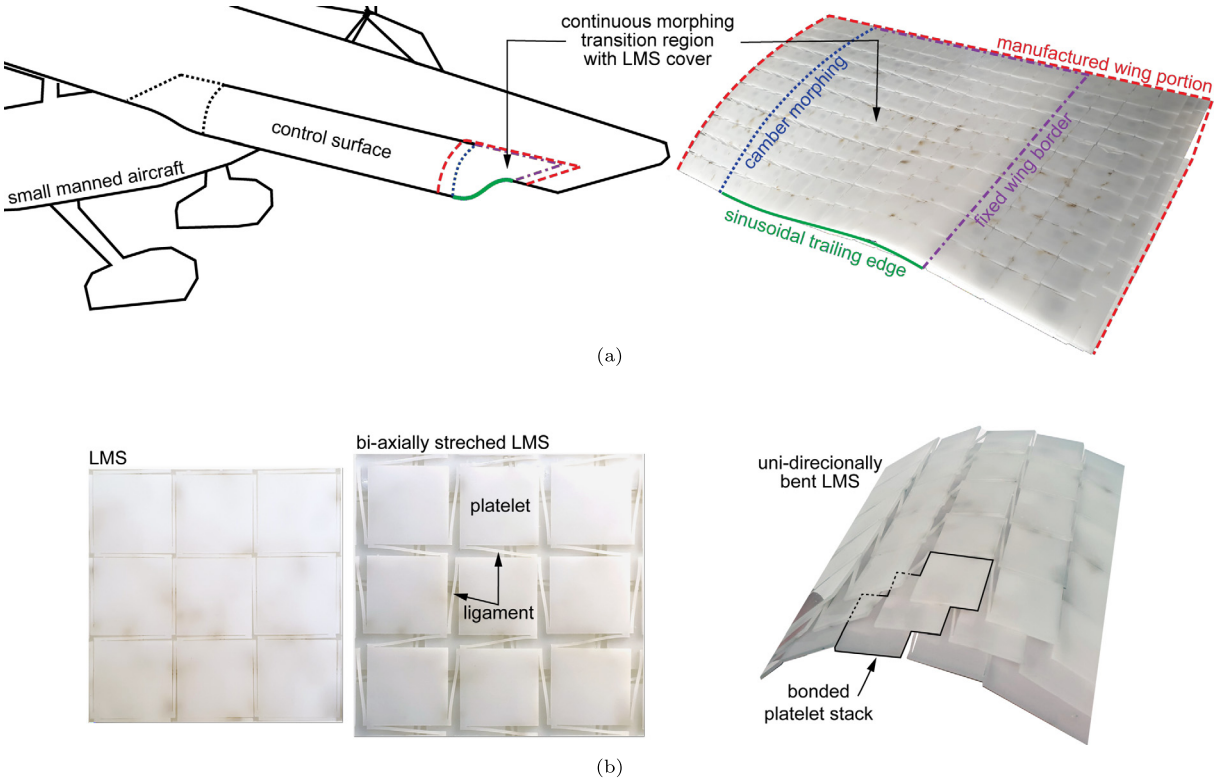

Fig. 1. Overview of the LMS application for a camber morphing transition region (a) and the fundamental skin deformations (b). (For interpretation of the colours in the figure(s), the reader is referred to the web version of this article.)

morphing concepts [26], the realisation of such a skin on a global wing scale is an enormous challenge. By limiting the application of the morphing skin to small areas where mass is secondary and to turbulent flow where skin roughness is of less importance, it is possible to combine large bi-axial deformability and extreme anisotropy in a morphing skin with an inherently closed surface. The realisation of such a concept extends the application range of morphing skins.

This work presents the layered morphing skin (LMS) concept applied to a continuous camber morphing transition region which smoothly connects a wing's camber morphing region to its fixed wing segment. The transition region subjects the skin to strains in shear, span and chord and links its deformed trailing edge to its straight edge upstream while being fully subjected to the wing's aerodynamic loads [3]. Numerical studies show that smooth transition regions reduce vortices [27] and increase the lift-to-drag ratio by 7.25% [3] compared to conventional slotted control surfaces. To date, pre-strained elastomeric sheets have formed the transition regions' aerodynamic surfaces [3,28].

The LMS is a highly anisotropic structural metamaterial based on stiff overlapping platelets interconnected through compliant ligaments. The structural elements contribute to high out-of-plane stiffness, two-dimensional in-plane compliance and large bi-axial deformability of the skin. The overlapping platelets provide a closed, albeit not perfectly smooth surface. This work focuses on the mechanical aspects of the LMS and a Cessna 172 Skyhawk is used to specify geometry and load requirements for the LMS, the camber morphing aileron, and the transition region connecting fixed wing and morphing aileron. Subsequently, the skin's design and manufacturing is presented. The LMS' deformations are analysed on the manufactured wing portion and the mechanical response of the LMS is investigated in detail.

2. Morphing concept

2.1. Skin, transition region, and requirements overview

The LMS developed throughout this work is a load-carrying skin which can undergo two-dimensional planar strains. The LMS' strain capabilities are demonstrated by covering a wing portion's pressure and suction side with the LMS. The wing portion itself consists of a camber morphing control surface, a continuous camber morphing transition region and a fixed wing segment (Fig. 1a). From Fig. 1a it is evident, that the LMS undergoes large strains in chord direction where chamber morphing is present and strains in span direction due to the extended arc-length of the morphed edge. This results in a two-dimensional strain field. Findings of Woods et al. [3] indicate that the trailing edge should approximate a sinusoidal shape to minimise undesirable flow phenomena. Additionally, the LMS undergoes large shape changes by linking the morphed trailing edge to the straight leading edge of the wing portion.

The LMS, consists of two geometric entities, namely slender, bending compliant ligaments and stiff platelets (Fig. 1b). The ligaments connect diagonally adjacent corners of neighbouring platelets, resulting in a grid-like layer (LMS layer). In-plane skin deformations are provided by the LMS layers' slender ligaments (Fig. 1) undergoing bending, while the platelets move relative to each other with rigid body motions. As bending is an energetically efficient deformation mode for slender structures [29], the LMS actuation forces quantified in Section 5.2 are low.

Three of LMS layers are stacked and shifted in-plane to cover the ligament gaps, eliminating holes in the skin. As every LMS layer deforms identically, platelets with the corresponding position in every layer can be bonded. This creates a stiff, bonded platelet stack (framed in Fig. 1b) which overlaps with adjacent platelet stacks. This reciprocal support among the platelet stacks creates the high out-of-plane stiffness of the LMS. When the LMS is bent,

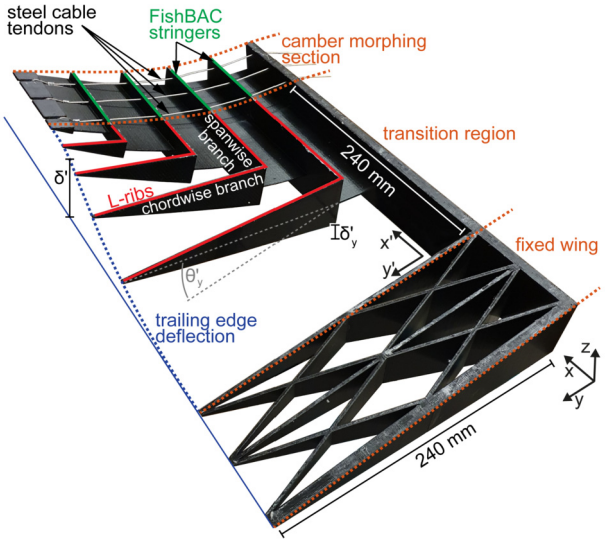

Fig. 2. Wing core, additively manufactured from PLA.

the bonded platelet stacks can only approximate a curvature which causes surface imperfections, which are investigated with respect to their aerodynamic impact in the course of this work.

From the Cessna 172 Skyhawk, a small manned aircraft, requirements and flow conditions for the LMS and the transition region of a camber morphing aileron are deduced to evaluate its performance. As the Skyhawk's detailed aileron dimensions are not publicly available, they are derived from a chord length of 1.13 m at the wing's tip [30]. Assuming a standard aileron design, occupying 15% to 25% of the tip's chord length [31], the aileron's chord needs to be between 17 cm and 28 cm. The aileron deflection ranges from 20° upwards to 15° downwards [32]. The extended flaps airspeed limit of 43.7 m/s, which corresponds to 66% of the maximum cruising speed [32], and a Reynold's number (Re) range from $2.6 \cdot 10^6$ to $3.5 \cdot 10^6$ along the aileron (not deflected) indicate a turbulent flow regime [33]. The flow conditions are used to determine the aerodynamic impact of the LMS' imperfections. For assessing the load carrying capabilities of the LMS, the air pressure on the morphing aileron and on the structural skin is assumed to be equivalent to the wing loading of 632 Pa [34]. This is a conservative assumption, as the pressure distribution is inhomogeneous over the wing's chord and decreases towards the trailing edge.

2.2. Camber morphing transition region design

The wing portion's core structure (Fig. 2) in this work is responsible for the desired morphing deformations and consists of three parts: the camber morphing section, the transition region and the fixed wing. The camber morphing section represents a narrow part of a morphing aileron. Upwards and downwards deflection is applied via three steel cable tendons on the top and bottom side of the section, respectively. The camber morphing section design is based on the FishBAC concept by Woods [35,36], where through-profile-thickness FishBAC stringers (green in Fig. 2) are connected by a bending compliant plate in chord direction. For the fixed wing segment, which is not optimised, a honeycomb structure was chosen to reduce material usage.

The manufactured wing's core chord length of 240 mm fulfils the dimensional requirements for a Cessna 172 aileron. The morphing chord of the camber morphing section occupies the last 33.3% of a NACA 0012 airfoil with 720 mm chord which exceeds the standard aileron design for small aircraft with a maximum of 25%. However, standard control surface design has only limited applicability for morphing ailerons as these do not deflect with a hinged mechanism. FishBAC designs were presented with onset of morphing at 35% and 76.6% of the chord length, both showing improved lift-to-drag ratios compared to a conventional flap [36–38].

The design goal of the transition region segment (Fig. 2) is to provide a close to sinusoidal trailing edge deflection, which is an ideal aerodynamic shape [3,27], and also out-of-plane support for the LMS. The transition region segment is inspired by the designs of Woods [3] and Pankonien [28]. It consists of L-shaped ribs (red in Fig. 2), whose spanwise branches are connected to the equidistantly spaced FishBAC stringers (green in Fig. 2). When the camber morphing section is actuated, the L-ribs undergo a rotation θ'_y which corresponds to the deflection angle of the camber morphing section's bending plate at the chord positions of the FishBAC stringers. The chordwise branch of the L-ribs levers and translates the rotation into trailing edge displacement. The deflection of the transition region's trailing edge, δ', is therefore composed of the displacement from rotation of the chordwise L-rib branch, and of the deflection from the bending plate, δ'_y, at the chord position of the L-rib's spanwise branch.

To generalise the transition region design, span and chord coordinates, x and y, within the transition region segment are normalised with respect to their maximum (240 mm each), hence $x', y' \in [0, 1]$. The normalised span position of a chordwise L-rib branch, x'_{rib}, is set by design to

$$x'_{rib} = \sqrt{y'_{rib}}, \tag{1}$$

where y'_{rib} is the chord position of the spanwise L-rib branch connected to the FishBAC stringer. Using a linear cantilever beam model with distributed loads, small-angle approximation, and Equation (1), the deflection, δ', of the transition region's trailing edge can be expressed by

$$\begin{aligned}\delta'(x') &= \frac{\delta'_y + \theta'_y \cdot (L' - y')}{\delta'_{max}} \\ &= \frac{x'^4(6 - 4x'^2 + x'^4) + 4x'^2(3 - 3x'^2 + x'^4)(1 - x'^2)}{3},\end{aligned} \tag{2}$$

where $L' = 1$ is the normalised chord length of the transition region. The variable $\delta' \in [0, 1]$ is normalised with respect to the maximum trailing edge deflection δ'_{max} to eliminate the stiffness in the beam model, which is only relevant for actuation forces, but not for the deformed shape of the transition region. Plotting Equation (2) reveals a close representation of sinusoidal curve, which is also experimentally confirmed in Fig. 9 of Section 4.

2.3. Layered morphing skin design

2.3.1. LMS layer design

An individual LMS layer is constructed from compliant ligaments connecting diagonally opposite corners of adjacent platelets (Fig. 3a). These form meander-shaped platelet-ligament sequences in x and y direction. Stretching an LMS layer in x-direction causes bending of the ligaments oriented in y-direction and a small relative displacement of the middle platelet column in negative y-direction. Stretching in y-direction leads to bending of the ligaments in x-direction and to a relative movement of the middle platelet row in positive x-direction. Despite the relative displacements of individual platelet rows and columns, the LMS layer shows a global poisson's ratio of $\nu = 0$ in both in-plane directions and globally decouples the strains ε_x and ε_y. This behaviour also applies to the assembled LMS with $n_z = 3$ stacked platelet layers.

The platelets are rectangular, of dimensions l_x by l_y, with thickness, t, and separated by the gap size, g, in the undeformed state of the LMS. The global size of a LMS layer is characterised by n_x

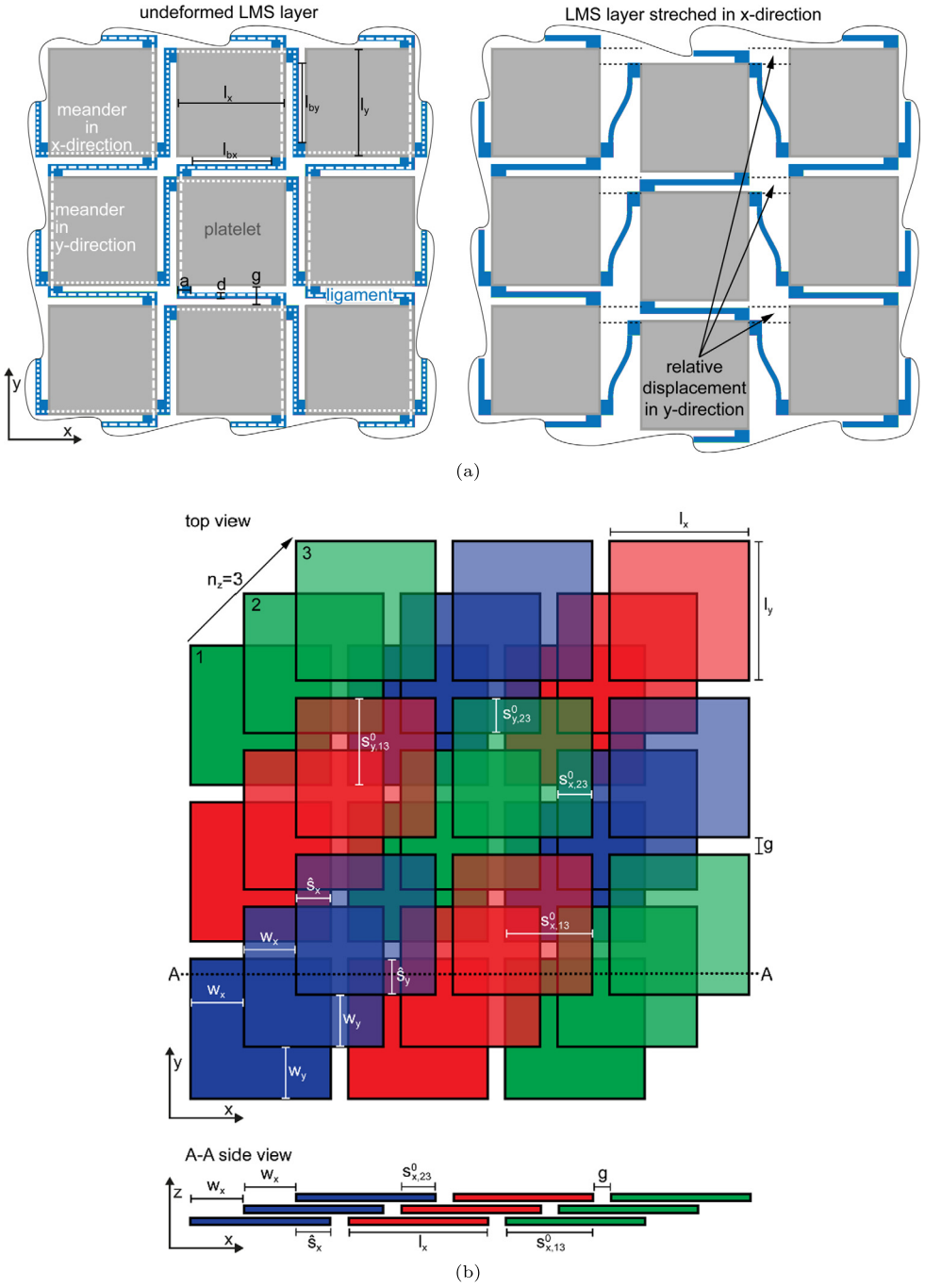

Fig. 3. Schematic design and deformation of an LMS layer (a) formed by a meander pattern of ligaments and platelets in x- and y-direction (white dotted and dashed lines, respectively). For the LMS with three layers (b), overlapping platelets of one colour are bonded and form a platelet stack which can move relative to the other stacks. For better readability the ligaments connecting the platelet stacks are not shown in (b). Sketches not to scale.

and n_y platelets in x- and y-direction, respectively. The parameters a and d describe the attachment length and width of the ligaments, while the ligaments' free lengths are calculated as

$$l_{bx} = l_x - 2a,$$
$$l_{by} = l_y - 2a. \tag{3}$$

All geometric layer parameters are also visualised in Fig. 3a.

In general, any bending compliant structure between the platelets could provide in-plane compliance. However, straight ligaments are easiest to manufacture and minimise the gap size, g, in the strain-free state of the LMS.

2.3.2. Three-layered LMS

A single LMS layer possesses a low out-of-plane stiffness and does not provide a closed surface. It is therefore unsuitable as an aerodynamic surface. Only the stacking and shifting of at least $n_z = 3$ layers (Fig. 3b) prevents the presence of holes in the skin. The relative shifts, w_x and w_y in x- and y-direction, of every LMS layer cause the platelets of different layers to overlap, closing the LMS surface. Platelets with corresponding positions in each layer are bonded together, creating rigid platelet stacks. Fig. 3b indicates those stacks with red, blue and green colour. In general, any number of more than three LMS layers can be stacked, but this work focuses on the simplest and thinnest geometry with $n_z = 3$ layers.

The variables $s_{x,ij}$ and $s_{y,ij}$ indicate the overlap lengths of adjacent platelet stacks between layers i and j with $i \neq j$ in x- and y-direction, respectively. As these overlaps shrink when the skin is stretched, a superscript '0' refers to the initial, undeformed state of the LMS, where the stack overlaps ($s^0_{x,ij}$, $s^0_{y,ij}$) are maximal. A superscripted '1' indicates the maximally morphed state of the LMS and the minimal stack overlaps ($s^1_{x,ij}$, $s^1_{y,ij}$) the LMS is designed for. Non superscripted overlap lengths refer to any morphing state. Moreover, the overlap lengths $\hat{s}_x$ and $\hat{s}_y$ are introduced, which do not change when the LMS is stretched in y- and x-direction, respectively. A hat on a variable indicates that it is constant over the morphing process of the skin. The aforementioned variables are all clarified in Fig. 3b.

The stack overlaps, $s^0_{x,ij}$, are calculated as

$$\begin{aligned} s^0_{x,13} &= 2w_x - g, \\ s^0_{x,23} &= w_x - g, \end{aligned} \tag{4}$$

and the constant stack overlap length $\hat{s}_x$ as

$$\hat{s}_x = l_x - 2w_x. \tag{5}$$

Equations (4) and (5) derive from the LMS geometry given in Fig. 3b. It follows directly from Equation (4) that

$$s^0_{x,13} \geq s^0_{x,23}. \tag{6}$$

As the overlaps lengths $s_{x,13}$ and $s_{x,23}$ shrink by the same amount when the LMS is stretched, the inequality holds for any morphing state ($s_{x,13} \geq s_{x,23}$). The critical stack overlap to prevent holes in the LMS for any morphing state is consequently $s_{x,23}$, which is used to define the design strain of the LMS, $\hat{\varepsilon}_x$. With an engineering strain definition

$$\hat{\varepsilon}_x := \frac{s^0_{x,23} - s^1_{x,23}}{l_x + g}, \tag{7}$$

where the difference, $s^0_{x,23} - s^1_{x,23}$, represents the total morphing displacement between adjacent platelets and $l_x + g$ the initial undeformed length.

It is evident from Fig. 3b that all stack overlaps must always be larger than zero to prevent holes in the LMS. The design choice made is that $\hat{s}_x$ and $s^1_{x,23}$ are set to be equally small with

$$\frac{\hat{s}_x}{s^1_{x,23}} = 1. \tag{8}$$

In general this ratio is freely selectable, but extreme ratios lead to either $\hat{s}_x$ or $s^1_{x,23}$ being close to zero. A ratio of 1 or slightly above is recommended for balanced stack overlaps.

Combining Equations (4), (5), (7), and (8), the design strain, $\hat{\varepsilon}_x$, can be written as

$$\hat{\varepsilon}_x = \frac{3w_x - g - l_x}{l_x + g}. \tag{9}$$

The geometry, l_x and g, as well as the design strain, $\hat{\varepsilon}_x$, can be selected to solve for the platelet shift w_x. Note that to prevent holes in the skin, it is required that

$$g < w_x < l_x/2. \tag{10}$$

Therefore the maximum allowable design strain is

$$\hat{\varepsilon}_{x,max} = \lim_{w_x \to l_x/2} \hat{\varepsilon}_x = \frac{\frac{1}{2}l_x - g}{l_x + g}. \tag{11}$$

Equation (11) converges for very small gap sizes g to

$$\lim_{g \to 0} \hat{\varepsilon}_{x,max} = 0.5. \tag{12}$$

For simplicity, Equations (4) to (12) are only presented in x-direction, but they equally hold in y-direction. In theory, an LMS can therefore change its surface area up to 125% by morphing 50% in each in-plane direction which is a large bi-axial deformation for a morphing skin. Practically, the design strain $\hat{\varepsilon}_x$ is limited such that the beam deformation is elastic. This is discussed further in Section 5.3.

2.3.3. Aerodynamic considerations

From Figs. 1 and 3 it is evident that the LMS does not exhibit a perfectly smooth surface. Gaps appear between the platelets when the LMS is stretched and steps occur where the platelets protrude from bending the LMS. Research on the aerodynamics of a corrugated surface placed in the aft 30% of the chord length of a NACA 0012 airfoil indicates that the aerodynamic costs can be nearly reduced to a no penalty situation [39]. Additionally, extensive research by Jacobs on the aerodynamic impacts of imperfections on airfoils shows that protuberances up to 0.5% of the total chord length do not significantly decrease the lift-to-drag ratio when placed at 65% chord behind the leading edge [40]. Jacobs' analysis was carried out for $Re = 3.1 \cdot 10^6$ which fits the Reynolds number range present for the Cessna aileron. In general, the loss of aerodynamic efficiency is the less pronounced the further downstream the protuberance is located and the more turbulent the flow is [40,41]. The surface of the LMS is expected to be aerodynamically sufficient, if the LMS is applied in a turbulent flow regime and does not exceed a protuberance size of 3.6 mm, which is confirmed in Sections 4 and 5.2.3.

Another consequence from the stacked and overlapping platelets is the absence of absolute air-tightness. The platelets form a stepped labyrinth seal with very limited cavities (gaps between platelets, Fig. 3b) where the airflow's kinetic energy is dissipated by turbulences [42]. Nevertheless, good sealing properties are expected, since the z-direction clearances between the stacked platelets due to manufacturing imperfections (Section 3.1.1) do not exceed 0.1 mm. The small ratio of clearance to stack overlap results in a low kinetic flow energy carry-over factor [43,44], indicating a low fluid leakage rate.

3. Methodology

3.1. Manufacturing

3.1.1. LMS manufacturing process

The LMS is manufactured in a two-step process. Each layer is separately cut with a CO_2 laser cutter (Trotec Speedy 400), stacked and consecutively bonded to its neighbouring layers. The processing route requires a material appropriate for laser-cutting that also exhibits a high toughness and yield limit, since the local strains and stresses in the ligaments can be considerable.

Polyoxymethylene co-polymer (POM-C), is a highly crystalline, machinable, rigid, tough, strong and dimensionally stable polymer [45,46] that exhibits excellent laser processability and fulfils the mechanical material requirements. An elastic modulus around 3 GPa with material density of $\rho = 1.4$ g/cm^3 [46] results in a low specific stiffness and is the major drawback of POM-C for weight critical aerospace applications. As the mechanical properties of POM-C, in particular the elastic modulus, E, can vary with the degree of crystallinity [47], material testing (Section 5.1) is necessary for extracting the exact tensile response which is used as input for the numerical analysis of the presented structures (Section 3.4). In order to create a thin platelet layer and LMS, the thinnest commonly available POM-C sheet material with a thickness of $t = 1$ mm is chosen.

Table 1
Geometric specification of manufactured LMS.

Parameters	Value	Unit	Description
l_x, l_y	20	[mm]	platelet size
l_{bx}, l_{by}	16.5	[mm]	free ligament length
d	0.7	[mm]	ligament width
a	1.75	[mm]	attachment length
g	0.9	[mm]	gap size in undeformed state
t	1.0	[mm]	layer thickness
n_z	3	[-]	number of layers
$\hat{\varepsilon}_x$, $\hat{\varepsilon}_y$	0.3	[-]	design strain
w_x, w_y	9.06	[mm]	shift per layer

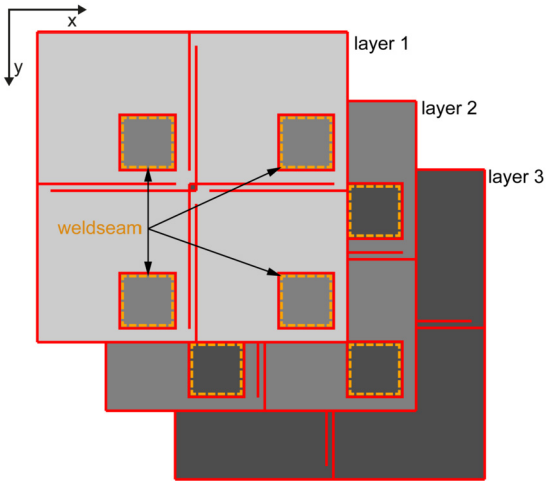

Fig. 4. Laser cut and assembly pattern of a $n_x = 2$ by $n_y = 2$ by $n_z = 3$ LMS with the geometry from Table 1. The individual laser cut layers (red lines represent cuts) are welded together along the cut out edges (dashed orange line), starting with the outermost LMS layers (layer 2 and 3). Figure is 1:1 scale.

Manufacturing trials for the LMS have shown that the Trotec Speedy 400 laser cutter reliably achieves a cut width of 0.1 mm and feature sizes down to 0.7 mm with the POM-C sheet material used. The ligaments are cut to the lowest manufacturable width ($d = 0.7$ mm, $g = 0.9$ mm) and the chosen platelet dimensions of $l_x = l_y = 20$ mm allow a manual LMS assembly. The global design strain is set to $\hat{\varepsilon}_x = 30\%$. The complete geometric specification is given in Table 1.

The low surface energy makes POM-C difficult to adhesively bond [48], therefore a layer-by-layer, thermoplastic welding concept, displayed in Fig. 4 is employed to assemble the LMS. All internal LMS layers (layer 1 and 2 in Fig. 4) possess square cut outs which fully overlap with the platelets of the next layer. The outermost layer (layer 3) is free of cut-outs. The assembly and welding along the cut outs' edges (Fig. 4) is carried out from outside (layer 3) to inside (layer 1). It is important to note that excessive molten POM-C from the weldseams can flow in between the platelets of one stack, separating them up to approximately 0.1 mm in z-direction. This vertical offset must be accounted for in the FE model (Section 3.4) for analysing the global mechanical response of the LMS system.

3.1.2. Wing section manufacturing

The manufactured wing portion consists of core structure (Section 2.2) and the LMS (Section 2.3) as a cover. The core is additively manufactured from Polylactic Acid (PLA) in three parts (camber morphing section, transition region and fixed wing) which are adhesively bonded after printing.

The skin cover, a 11 by 20 platelet LMS with geometry as specified in Table 1, is manufactured from POM-C. The LMS is pre-strained by 10% in chord direction to accommodate compressive strains resulting from camber morphing. The skin is manually bonded to the fixed wing section with double-sided adhesive tape (3M VHB Tape LSE for low surface energy surfaces). Successively following the span of the wing portion's core (x-direction, Fig. 2), the LMS is attached to the L-ribs of the transition region and then to the FishBAC stringers. During fitting of the LMS in span direction, little pre-strain ($\approx 3\%$) is applied to compensate manufacturing and positioning imperfections.

Fig. 5. Tensile coupon geometry according to ISO 527 [49].

3.2. Wing section deformation measurements

The camber morphing section of the manufactured wing portion with LMS is deflected upwards and downwards by loading the respective steel cable tendons with a total force of 70 N. The deformation of the whole wing portion is tracked on the LMS' surface with a digital image correlation system (DIC) by equipping the platelets of the outermost LMS layer with speckle pattern targets. The platelets undergo rigid body motions as the deformation is localised to the slender ligaments. Hence, the DIC allows measurements of global deformations, but not of the localised ligament deflections.

While the displacements of the platelets can be directly extracted during image post-processing, the strains present in the LMS, ε_x and ε_y, are derived from the relative displacements of the individual platelet stacks. The strains, ε_x and ε_y, are evaluated analogous to Equation (7) by dividing the relative movement between two neighbouring platelets by the undeformed length $l_x + g$.

3.3. Mechanical testing of the layered morphing skin

3.3.1. POM-C tensile test

For the material characterisation of POM-C, five dog-bone shaped tensile test coupons are laser-cut from the POM-C sheet material. Their dimensions, according to DIN ISO 527 [49], are given in Fig. 5. The deformation rate of the Zwick-Roell tensile testing machine (5 kN loadcell, 0.05 N accuracy) is set to 0.8 mm/s and the specimens are tested until failure. A digital-image-correlation (DIC) system tracked the strains and displacements of a 50 mm gauge length within the parallel mid-section of the dog-bone specimens.

3.3.2. Unidirectional LMS tensile test

When evaluating the mechanical response of a morphing skin system, the anisotropy of in-plane compliance and out-of-plane stiffness, as well as the shear stiffness are the main mechanical properties. A unidirectional tensile test on the LMS is carried out to evaluate the in-plane actuation forces. A LMS specimen with 5 by 5 platelet stacks is manufactured with the dimensions from Table 1 and clamped at opposite ends. The clamps of the strain free specimen are attached to the Zwick-Roell tensile testing machine (crosshead speed 0.5 mm/s). The DIC system tracks the deformation of the specimen via speckle patterns applied to the platelets with a sample rate of four frames per second, while the load cell measures the reaction force of the specimen. The specimen is loaded until failure.

3.3.3. LMS shear test

The LMS' shear response is dependent on its in-plane pre-strain (Section 5.2.2) and is therefore evaluated for three unidi-

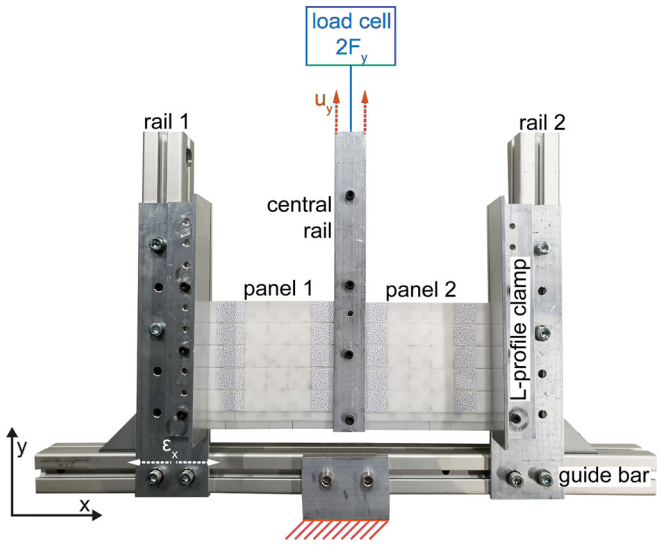

Fig. 6. Shear test set-up.

Table 2
Pre-strain, ε_x, of tested shear panels.

ε_x [%] desired	ε_x [%] panel 1	ε_x [%] panel 2	ε_x [%] average
10.0	10.3	10.5	10.4
20.0	20.0	20.6	20.3

rectional pre-strains, $\varepsilon_x \in [0\%, 10\%, 20\%]$. A three-rail shear testing rig (Fig. 6) allows for manual, uni-directional pre-straining of the specimens, provides accurate shear forces [50,51] and keeps the load cell free of shear loading. The reported shear forces are the average of the shear force of the two panels.

Two mirror-symmetric, 5 by 5 platelet LMS panels are manufactured for each pre-strain, equipped with printed speckle patterns along the outermost platelet columns, and clamped to the central and outer rails 1 and 2 of the shear testing rig (Fig. 6). The pre-strain, ε_x, is applied by sliding and fastening the rails 1 and 2 along the guide bar until the desired ε_x is reached.

The DIC system tracks the vertical shear deformation, u_y, and the horizontal displacement, u_x, of the speckled platelets which allows to extract the exact pre-strains, ε_x, tabulated in Table 2. The cross-head speed of the tensile testing machine was set to 0.5 mm/s and the capture rate of the DIC was four frames per second.

3.3.4. LMS out-of-plane pressure test

The resistance against out-of-plane forces is needed to quantify the LMS' anisotropy and aerodynamic load carrying potential. Out-of-plane load is applied to a biaxially pre-stretched LMS through a hydrostatic pressure test. For reducing boundary condition effects, one large 8 by 8 platelet LMS is manufactured. The platelet stacks at the edges of the LMS panel are extended for fixation to the testing rig. The LMS is tested with three different pre-strains to determine the strain dependency of the out-of-plane response.

The outermost extended platelet stacks are clamped with the L-profile clamps 1 and 3 in Fig. 7 and the LMS' pre-strain, ε_x, is applied by sliding and fixing the L-profile clamps 1 and 3 in the slots of the guide plate. To apply the pre-strain ε_y, the L-profile clamps 2 and 4 are added to the free edges of the LMS and the clamp pair 1 and 3 can be removed, as the closed clamps 2 and 4 prevent contraction of the LMS in x-direction. Moving the clamps 2 and 4 along their slots in the guide plate and fixing them applies the pre-strain ε_y. Finally, the clamps 1 and 3 are reattached to the LMS and guide plate. The pre-straining process results in a uniform, two-dimensional strain state of the LMS (Table 3). The

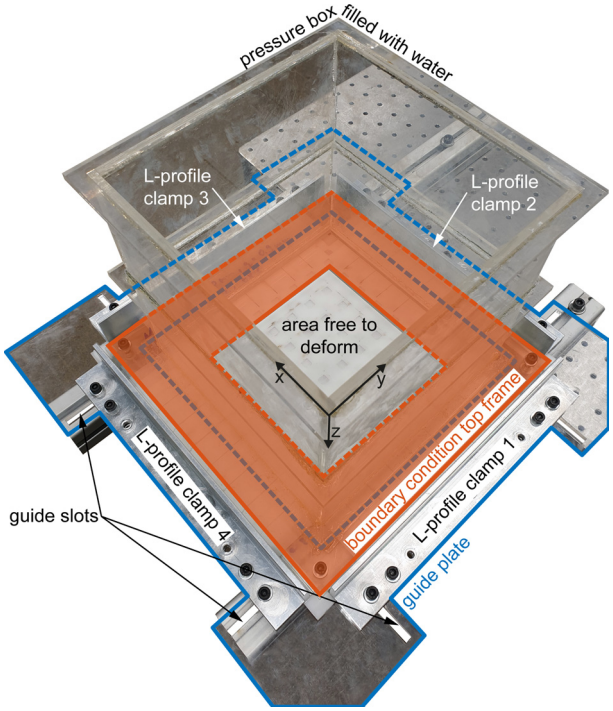

Fig. 7. Pressure test set-up made from transparent acrylic glass panels and aluminium clamps.

Table 3
Pre-strains, ε_x and ε_y, of tested LMS panel under pressure.

ε_x, ε_y [%] desired	ε_x [%] actual	ε_y [%] actual	ε_x, ε_y [%] average
10.0	11.0	10.4	10.7
20.0	19.5	19.4	19.5

pre-strained state of the skin, as well as its out-of-plane deformation during the pressure tests, is evaluated with the DIC system.

For the hydrostatic head which represents the aerodynamic forces, water is filled up to 20 cm high into a pressure box equipped with a loose plastic liner. The out-of-plane deformation of the morphing skin is captured at every 5 cm of increasing water level (corresponding to pressure levels of 490.5 Pa). The clamped boundary condition at the edges of the LMS panel is realised by positioning the LMS specimen between two frames (orange in Fig. 7), which keep the outermost platelet stacks in place.

3.4. FE model of the layered morphing skin

To capture the global mechanical behaviour and the deformation modes of the LMS in more detail, an FE model is created with ABAQUS standard v6.14. The three layered LMS is created by attaching individual LMS layers using tie constraints. The platelets of the LMS layer are represented with twenty-node, quadratic C3D20R solid elements with reduced integration and the ligaments are modelled with three-node, quadratic B32 beam elements. The attachment length of the compliant beam, a, is used as the platelets' mesh size, the ligament beam's mesh size corresponds to $\min\left[(l_x - 2a)/20, (l_y - 2a)/20\right]$. This results in a coarser mesh with one solid element through thickness for the platelets and a finer mesh of 20 beam elements for the ligaments. A mesh study revealed that for the given structure and load cases, convergence is achieved with the specified quadratic meshes.

The ligaments' ends are coupled to their platelets via multi-point-constraints (ABAQUS' MPC constraint). Additionally, hard and

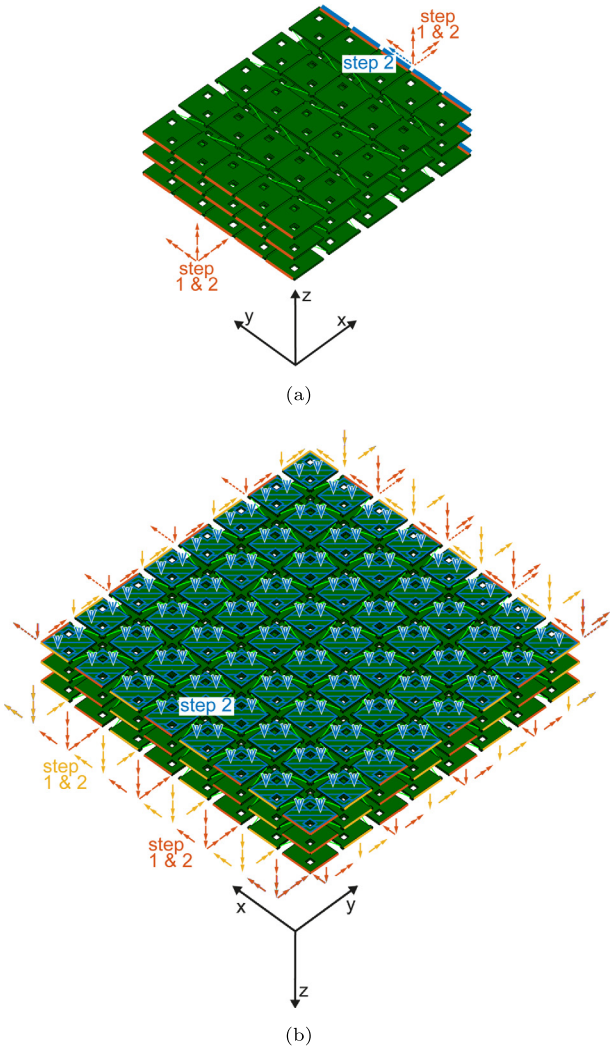

Fig. 8. Boundary conditions (BCs) and loads for (a) shear and (b) pressure simulations. Solid arrows and solid double arrows indicate the blocked translational and rotational degrees-of-freedom, respectively. They act on the platelet stacks' side faces. Dashed arrows indicate applied displacements and hatched areas pressure. Orange and yellow colours imply application of the BCs in the pre-straining step 1 and retaining them in the load step 2, whereas blue colour indicates application of the loads in load step 2. (a) is displayed with a pre-strain $\varepsilon_x = 0.203$ and (b) with $\varepsilon_x = \varepsilon_y = 0.195$.

tangentially frictionless contact is defined among the LMS layer's platelets for capturing potential in-plane contact.

As one LMS layer is copied to generate the LMS, all platelets in the simulation possess the cut-outs which are used in the manufacturing process to weld the LMS layers together (cf. Section 3.1.1). The simulation also supports stacking sequences other than presented in this work and for this reason the platelets exhibit two welding cut-outs which causes small holes in the LMS (Fig. 8). However, this is irrelevant, since only mechanical, but not aerodynamic behaviour is assessed with the FE simulation.

The generated LMS layers are stacked and shifted according to the design criteria presented in Section 2.3.2. A clearance of 0.1 mm between the LMS layers is introduced to account for manufacturing imperfections stemming from the welding process. Tie constraints between the platelets' cut-out edges represent the weldseams (cf. Fig. 4). Hard and tangentially frictionless contact is introduced between all neighbouring LMS layers to prevent the platelet stacks from penetrating each other in out-of-plane direction.

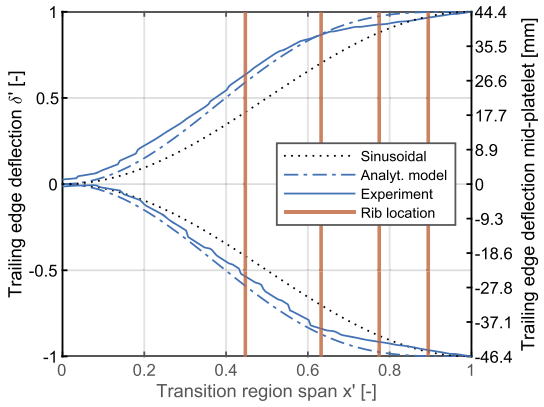

Fig. 9. Trailing edge deflection comparison between linear beam model and mid-platelet measurement. Axes normalised to maximum deflection and span of the transition region. Orange lines indicate the position of the L-ribs' chord oriented branch.

The simulation of shear and pressure response is analogous to their experimental evaluation (Section 3.3) and consists of two steps. In a first quasi-static load step with non-linear geometry, the clamped boundary conditions and pre-strains, both explained in more detail with Fig. 8, are applied. Consecutively, the skin is subjected to shear displacement (blue dashed arrow in Fig. 8a), or pressure (blue hatched areas with blue arrows in Fig. 8b) during a consecutive load step (quasi-static, non-linear geometry). In order to validate the simulations, reaction forces, F_y, and out-of-plane deflection, u_z, are analysed for shear and pressure simulation, respectively. For simulating the tensile test, the first load step of the shear simulation with a pre-strain up to $\varepsilon_y = 0.8$ is used.

4. Deformation of transition region employing the LMS

This section analyses the wing portion with the LMS cover to characterise the transition region deformation in response to camber morphing. The analytical model for trailing edge deflection, presented in Section 2.2 and displayed with a blue dashed-dotted line in Fig. 9, approximately represents a sinusoidal shape (black dotted lines) and matches the experimentally measured trailing edge deflection (blue solid line). The model does not consider the rigid nature of the platelet stacks which can only approximate curvature as straight segments. Therefore, the measured curve exhibits less curvature than the analytic model predicts, particularly between 70% and 90% of the transition region's span.

The small steps which are visible in the experimental trailing edge displacement curves result from the stiff platelet stacks not being able to fully undergo the desired curvature, which is then compensated by out-of-plane bending of the ligaments and protrusion of the topmost platelet of each platelet stack. Due to the stacking of the platelets in positive x- and y-direction this phenomenon is particularly noticeable for the downward deflection curve. The maximum imperfection step size of protruding platelets is 2 mm, which is below the 3.6 mm determined as aerodynamically critical protuberance (Section 2.3.3). Additionally, the steps between the platelet stacks are oriented parallel to the airflow direction (in chord direction), which causes less drag compared to a protuberance facing the airflow. With the protrusion of platelets being maximal at the trailing edge, the surface smoothness achieved with the LMS is considered to be sufficient for turbulent flow conditions at this stage. However, future detailed aerodynamic investigations are required to characterise the precise effect.

The transition region's trailing edge deflection is evaluated along the mid-line of the platelets. Its maximal deflections of

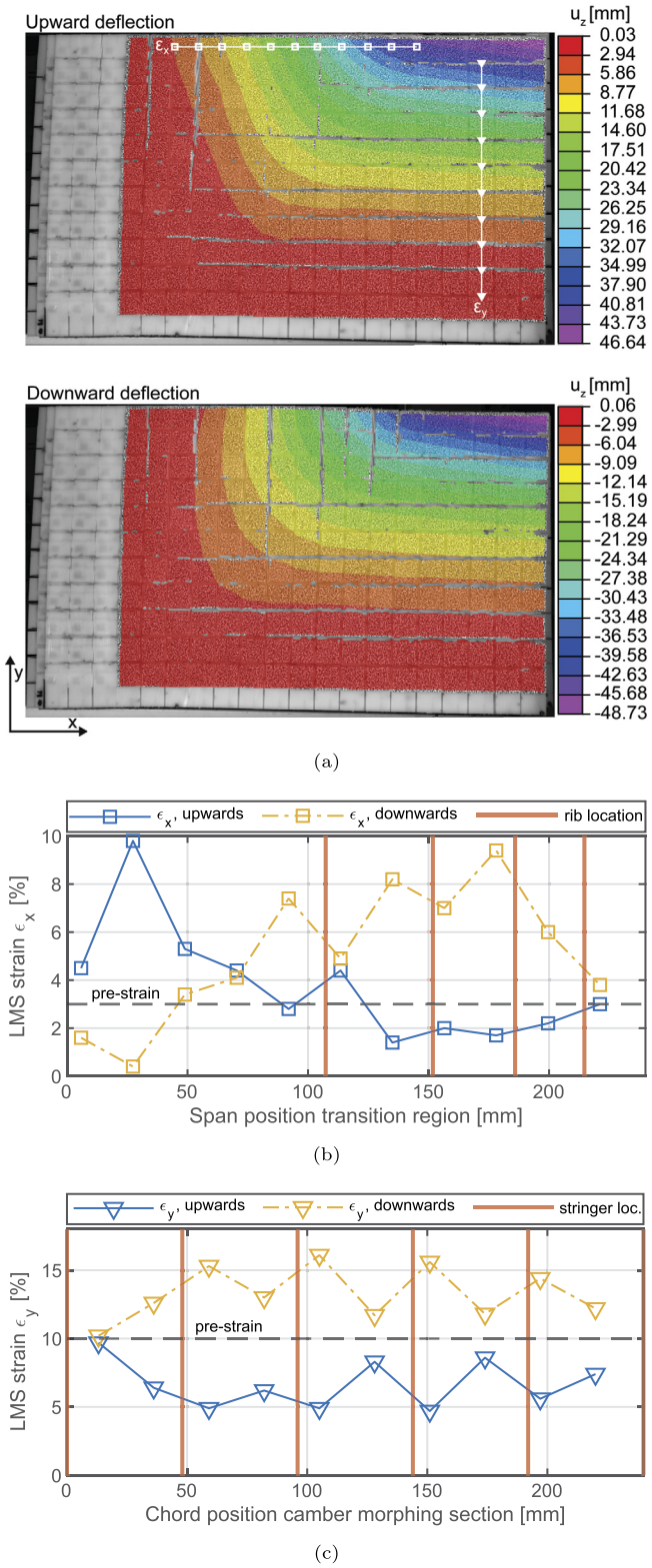

Fig. 10. Morphing deformation of wing portion, actuated with 70 N (a) with resulting trailing edge strains, ε_x, (b) and camber morphing strains, ε_y, (c).

44.4 mm upwards and -46.4 mm downwards (Fig. 9) are therefore smaller than the 46.6 mm and -48.7 mm measured globally at the actual trailing edge of the camber morphing section (pink areas in Fig. 10a). The maximum deflections correspond to 19.9% and 20.3% of the chord length of the wing portion. In aerodynamic studies of the FishBAC [36], Woods et al. have shown that a traditional hinged flap with deflections of up to 30° produces a lift characteristic similar to a FishBAC camber morphing flap deflected by 12% of the chord length (corresponding to 28.8 mm for the camber morphing section in this work). Therefore it can be concluded that the deflections achieved with the manufactured wing portion are sufficient for the Cessna 172.

For the strains in span direction, ε_x, which are evaluated where marked with a white square in Fig. 10a, it is evident that in the concave curvature of the trailing edge tensile stresses appear, whereas for the convex curvature compressive strains appear (lines drop below 3% pre-strain, Fig. 10b). This is counterintuitive from experience, as tensile stresses would be expected for a convex shape. However, the combination of rib support, stacking sequence, and shear deformation that the LMS undergoes in the transition region cause the maximum strain $\varepsilon_x = 9.8\%$ where the LMS is concavely shaped. The shear deformation pattern is explained in more detail with the shear response of the LMS in Section 5.2. Note that in order to show the effect of the rib support, the measurement points in Fig. 10b are shifted by $-2w_x = -18.12$ mm which corresponds to the ligament positions of the bottom LMS layer that is connected to the L-rib.

Shear deformation of the LMS within the transition region is also the reason for an actuation force which is relatively high given the planar compliance of the LMS. The shear response of the LMS (Section 5.2) reveals that the LMS' shear stiffness is high but decreases drastically with application of pre-strain. Therefore, lower actuation forces can be achieved by larger bi-axial pre-strains.

It is evident, that the chordwise strains, ε_y, in Fig. 10c oscillate. The triangular markers in Fig. 10a indicate the measurement locations. Lower deviation from the pre-strain of 10% occurs when an unsupported platelet stack follows a platelet stack which is supported by a FishBAC stringer. Higher deviations show, where they are measured between an unsupported platelet followed by a supported one. The maximum strain $\varepsilon_y = 16.1\%$ (4th measurement point of yellow line in Fig. 10c) is present for the downwards camber morphing, where the change in strains adds to the pre-strain. This is also the strain which the ligaments must be able to provide, which is investigated in Section 5.3. The minimum strain is $\varepsilon_y = 4.7\%$ (6th measurement point of the blue line).

Overall, the wing structure and its analysis indicate that the developed morphing skin concept exhibits deformations suitable for a Cessna 172 transition region. The LMS is able to undergo two-dimensional strains and shows excellent out-of-plane stiffness, which is quantified in Section 5.2.3. The wing's surface is fully closed and exhibits localised imperfections which are not expected to severely disturb the aerodynamic properties when used in a turbulent flow regime.

The wing has not been weight optimised and has a total mass of 1.37 kg, where 0.40 kg are contributed by each LMS cover. When the LMS is applied locally and only where bi-axial strains are required, as present in the transition region, the weight contribution of the LMS is very small with respect to the aircraft's mass.

5. Mechanical performance of the layered morphing skin

5.1. POM-C characterisation

The results acquired from the material tensile tests, which are used in the FE simulation are displayed in Fig. 11. They agree well with values reported in literature [46,52], with an initial Young's modulus of 3.05 GPa being identified between 0.05% and 0.25% engineering strain and pure plasticity above stress levels of 65 MPa. Application of the standard yield criterion with 0.2% residual strain to the measured data results in a proof stress of 37.5 MPa, whereas POM-C datasheets [53,54] state the proof stress to be exactly coinciding with the ultimate tensile strength (UTS). For this work,

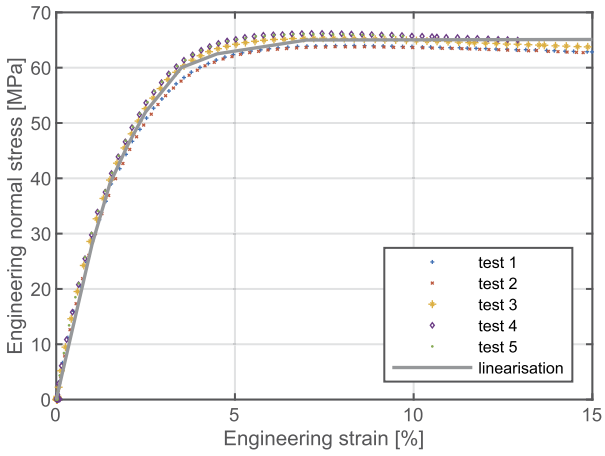

Fig. 11. Tensile test results and their multi-linearisation.

Table 4
Multi-linearisation of the material's tensile response in Fig. 11.

Engineering strain intervals [%]	Young's / secant modulus [MPa]
[0, 1]	2800
]1, 1.5]	2200
]1.5, 2]	1400
]2, 2.5]	1200
]2.5, 3.5]	800
]3.5, 4.5]	250
]4.5, 7]	100
]7, 15]	1.25

the manufacturer's data is used and the yield stress set to 65 MPa which corresponds to the UTS of the tested tensile coupons.

When the multi-linearisation (Table 4) used for the FE-model (Section 3.4) is compared to the tensile response of POM-C, it is evident that a Young's modulus of 2800 MPa is chosen over a one percent strain interval. This results in a more accurate tensile response of the FE model for the LMS when compared to experimental data (Section 5.2.1).

5.2. Mechanical response of the layered morphing skin

A detailed mechanical analysis in this section determines the anisotropy, load carrying capabilities and shear deformation pattern of the LMS. The LMS air sealing properties are briefly investigated with the LMS' deformed shape from the finite element analysis.

5.2.1. Tensile response

Fig. 12a depicts the tensile response of the $n_x = 5$ by $n_y = 5$ LMS with three layers. Below strains of $\varepsilon_x \leq 10\%$, the LMS simulation and experiment coincide and exhibit a linear behaviour. An equivalent in-plane Young's modulus, E_{eq}, is introduced for comparison purposes as

$$E_{eq} = \frac{F_y}{A_{cx}\varepsilon_y} = \frac{F_y}{n_z t\left[(n_x - 1)(l_x + g) + l_x\right]\varepsilon_y} = 198.0 \text{ kPa}, \tag{13}$$

where A_{cx} stands for the cross-sectional area of the LMS with the surface normal pointing x-direction. A reference linear elastic, isotropic and monolithic material of equivalent in-plane Young's modulus E_{eq} is also depicted in Fig. 12a (purple dashed line).

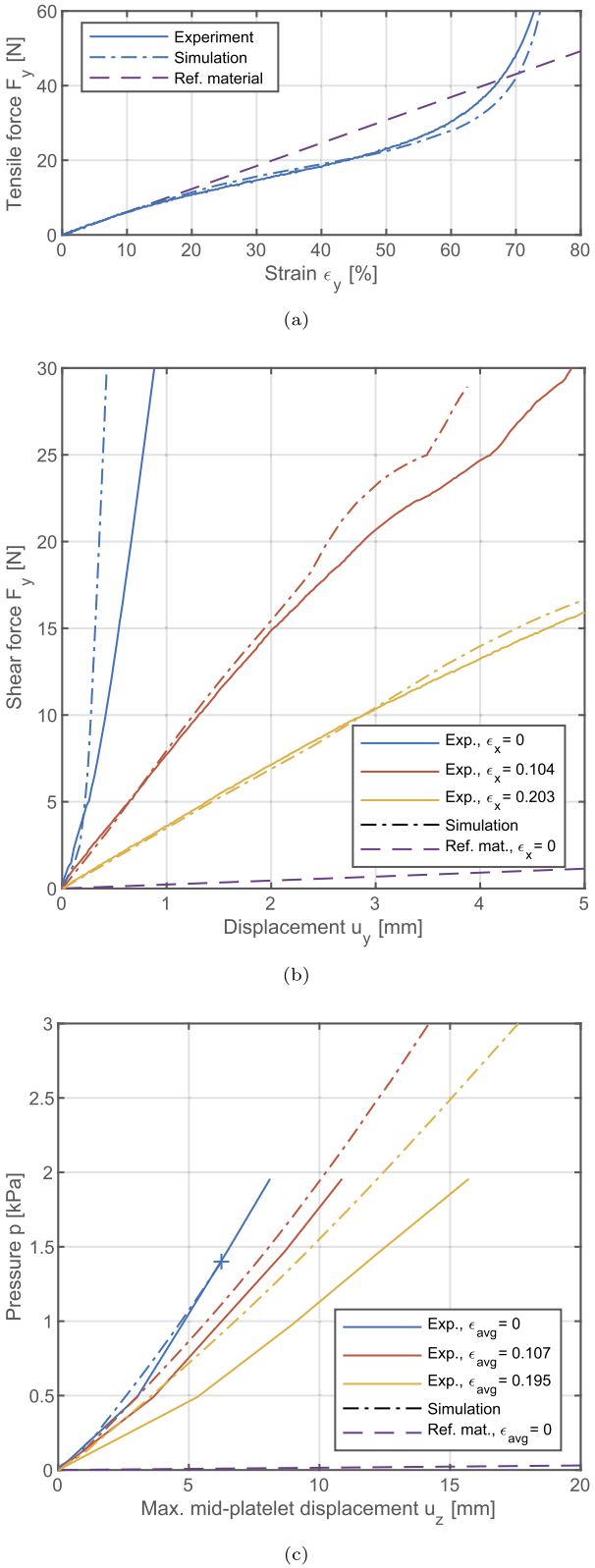

Fig. 12. Experimental tensile, (a), shear, (b), and pressure, (c), response (solid lines) of the LMS compared to the corresponding simulations (dashed-dotted lines) and an equivalently in-plane stiff, monolithic and isotropic material (dashed lines).

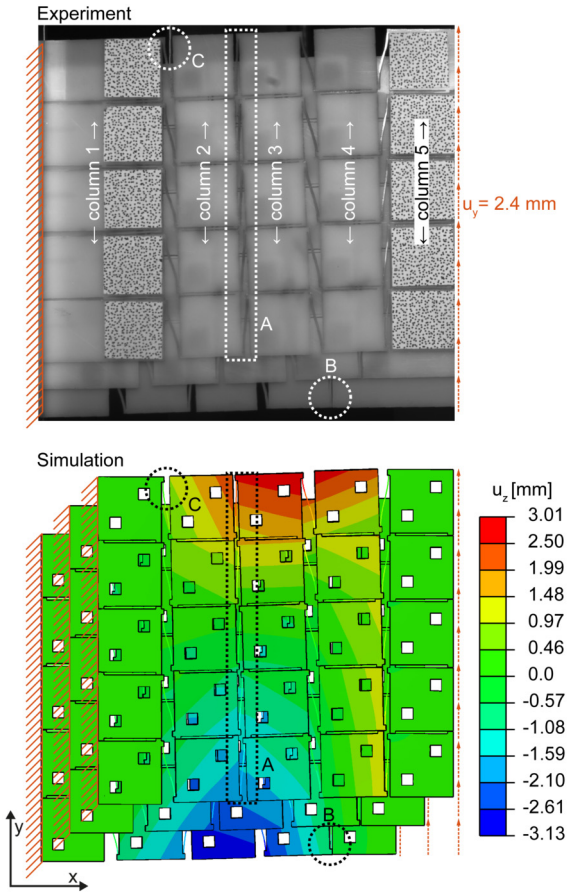

Fig. 13. Shear deformation comparison of experiment and simulation for an uni-axial pre-strain of $\varepsilon_x = 0.104$.

At higher strains, $10\% < \varepsilon_y \leq 40\%$, the deformation and stresses in the ligaments increase, meaning geometric non-linearities and the decrease in material stiffness (cf. Fig. 11) lead to a degressive tensile response. At large strains, $\varepsilon_y > 40\%$, the compliant beams connecting the platelets have undergone significant rotations. In this state the ligaments are loaded predominantly with normal tensile forces, which leads to a stiffening response.

The tensile response is relevant up to the design strain, $\hat{\varepsilon}$. In this range, the LMS' in-plane stiffness corresponds to a very soft elastomer [55] which shows potential for large deformations with low actuation energy.

5.2.2. Shear response

The LMS' shear stiffness contributes to the actuation forces of the camber morphing transition region due to the shear deformations present (Section 4). When subjected to shear displacement, u_y, the vertically oriented ligaments of the LMS in Fig. 13 are alternately loaded in tension (between platelet columns 2 and 3, and columns 4 and 5) or compression (between platelet columns 1 and 2, and columns 3 and 4). Ligaments under tension straighten and reduce the distance between neighbouring platelet columns, leading to their clustering (region A, Fig. 13). The distances of platelet columns that are connected by ligaments under compression increase with shear displacement.

The application of shear deformation, u_y, also causes the rotation of columns 2, 3 and 4 around the z-axis, which eventually leads to contact of platelet stacks in areas B and C and increases shear stiffness. For an LMS without pre-strain, $\varepsilon_x = 0$, this contact happens immediately and results in high shear stiffness (blue lines in Fig. 12b), whereas contacts are initiated at a force levels $F_y = 18$ N and $F_y = 25$ N for a pre-strain of $\varepsilon_x = 10.4\%$ which causes kinks in the shear response (orange lines in Fig. 12b). For large pre-strains, ε_x, no contact is initiated (yellow lines in Fig. 12b). In general, it holds that the shear response of the LMS follows a roughly linear trend and the shear stiffness reduces more than one order of magnitude when the pre-strain is increased to $\varepsilon_y = 20.3\%$. The simulations represent the trend of the shear response of the LMS, but behave slightly stiffer particularly for small pre-strains where manufacturing imperfections have a larger effect.

For the camber morphing transition region and applications where shear compliance is beneficial, it is recommended to apply significant pre-strain in span direction to reduce shear stiffness. However, with a pre-strain of $\varepsilon_x = 20.3\%$ the shear stiffness of the LMS remains one order of magnitude larger compared to the reference isotropic material (dashed purple line in Fig. 12b). The shear stiffness, G_{eq}, of the reference isotropic material is derived with an assumed Poisson's ratio of $\nu_{eq} = 0.3$ and first order, linear shear theory as

$$G_{eq} = \frac{E_{eq}}{2(1+\nu_{eq})} = 76.2 \text{ kPa}. \tag{14}$$

Due to the generally high shear stiffness, the LMS can contribute to the global shear stiffness of an adaptive structure, in particular the torsional rigidity of a morphing wing.

5.2.3. Pressure response

Similar to the shear load case, the out-of-plane stiffness anisotropy of the LMS is compared the reference isotropic material. Depending on the pre-strains, ε_x and ε_y, the LMS out-of-plane stiffness (see Fig. 12c) is at least two orders of magnitude higher than the equivalent isotropic material and shows the LMS' extremely anisotropic behaviour.

The maximum deflection at mid-point, $u_{z,eq}$, of a square isotropic plate uniformly loaded with pressure p and built-in edges is calculated with plate theory [56] as

$$u_{z,eq} = 0.00126 \frac{pb^4}{D}, \tag{15}$$

where b represents here the side length of the square and D the bending stiffness

$$D = \frac{E_{eq} h^3}{12(1-{\nu_{eq}}^2)}, \tag{16}$$

with $h = n_z t = 3$ mm being the plate's thickness. In order to make the comparison conservative, b is chosen not the same size as the 8 by 8 platelet stacks LMS panel, but smaller and the same size as the 6 by 6 platelet stacks of the LMS that are not directly affected by the applied boundary conditions in the pressure test (cf. Fig. 8b and 14).

The maximum mid-platelet deflection of the LMS (Fig. 12c) under pressure increases with its pre-strain. This primarily results from the fact that the surface area and therefore the total load on the LMS increases quadratically with bi-axial pre-strain. Hence, zero pre-strain $\varepsilon_{avg} = 0$ results in the stiffest behaviour (blue lines in Fig. 12c), and the highest pre-strain, $\varepsilon_{avg} = 0.195$ leads to the largest mid-platelet deflection.

There are two important aspects to note at this point. As evident from area A in Fig. 14, the maximum mid-platelet out-of-plane deflection is not located in the centre, but at the outermost corner of each tilted platelet stack. However, the platelets' corners cannot be tracked with the DIC and the difference in displacement, u_z, is small. Hence the maximum mid-platelet deflection is analysed in Fig. 12c. Secondly, the boundary conditions in the experiment cannot be applied as rigidly as in the simulations, resulting in a more tilted state of the outer platelets (e.g. areas B in

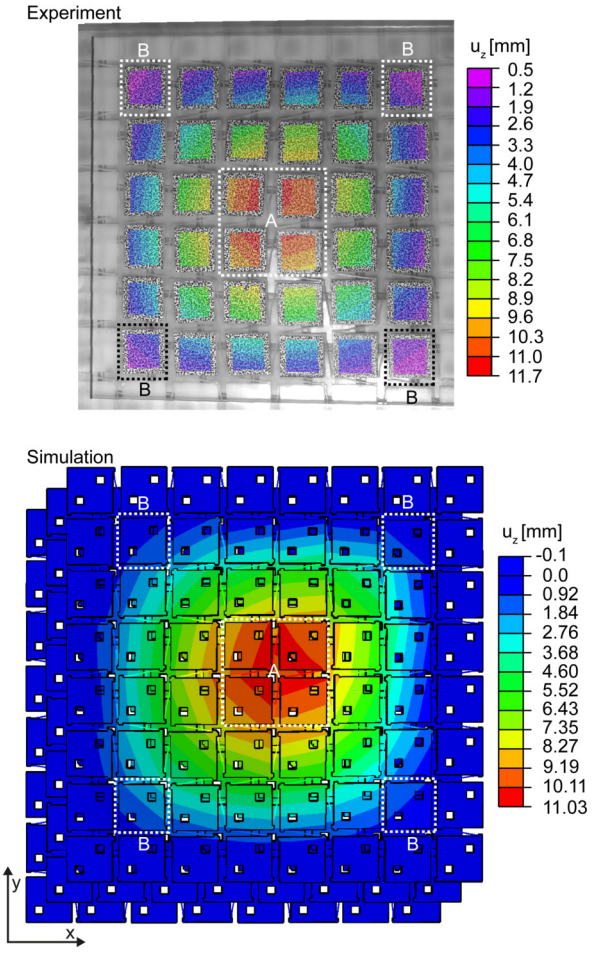

Fig. 14. Out-of-plane displacement, u_z, comparison of experiment ($\varepsilon_x = 0.110$, $\varepsilon_y = 0.104$) and simulation ($\varepsilon_x = \varepsilon_y = 0.107$) for an applied pressure of 1.98 kPa.

Fig. 14). This tilt angle leads, with increasing pre-strain and span, to larger deflections in the centre of LMS.

The validated FE model is used to examine the aerodynamic and labyrinth sealing properties of the out-of-plane deformed LMS. The largest unsupported LMS area in the transition region is between the fixed wing and the chordwise branch of the first L-rib (cf. Fig. 2) with 3 by 11 unsupported platelets stacks. A 5 by 11 platelet stack LMS with clamped boundary conditions on three sides (Fig. 15) is used to represent the unsupported LMS area of the wing section. With pre-strains according to the manufacturing process of $\varepsilon_x = 3\%$ and $\varepsilon_y = 10\%$, and the Cessna 172's wing load of 632 Pa, the maximum deflection is $u_z = 1.19$ mm at the trailing edge which corresponds to the A-A side view in Fig. 15. Keeping in mind that the aerodynamic protuberances should stay below 3.6 mm (Section 2.3.3), the LMS fulfils this criterion. Therefore, it is deducted that the LMS made from POM is a sufficiently out-of-plane stiff aerodynamic cover of the camber morphing transition region and applicable to a Cessna 172 Skyhawk.

From the side view in Fig. 15 it is also evident, that the out-of-plane deformation of the LMS does not influence all clearances between the platelet stack overlaps. This means the labyrinth sealing properties of the LMS are similar to its undeformed state with low kinetic flow energy carry over factor (Section 2.3.3) and leakage rate expected. It can be assumed at this point, that the LMS sealing properties are suitable for a camber morphing transition region, but a detailed leakage analysis is necessary in future work.

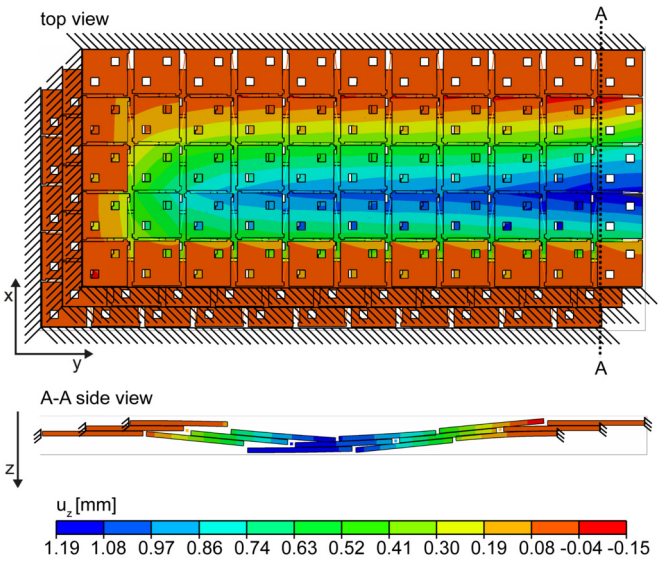

Fig. 15. Out-of-plane deformation at 632 Pa of the LMS representing the largest unsupported area of the manufactured wing section. The displacement u_z is scaled with a factor of 3 in the A-A side view.

5.3. Ligament plastification

During the experiments with the manufactured wing section, small permanent deformations of the LMS ligaments were observed, particularly where the chordwise strain is highest with $\varepsilon_y = 16.1\%$. Although not influencing the functionality of the demonstrator, plastic deformations can be undesired for aerospace applications, since the skin must undergo many load cycles. Therefore a plane-stress FE model with a fine mesh of quadratic CPS8R elements (minimum element size 0.01 mm) is employed to assess the notch effect of the laser cuts and the stresses within the ligaments.

Fig. 16a shows the von Mises equivalent stresses of the standard ligament with the geometric specifications from Table 1 under a unidirectional strain of $\varepsilon_y = 0.161$. When using a plastification stress level of $\sigma_{plast} = 65.0$ MPa as specified in Section 5.1, the ligament exhibits very localised plastic deformation at the point of stress concentration caused by the laser cut notch. Additionally, stresses close to 65.0 MPa, which are independent of the notch effect, occur at the root of the ligament and can cause plastic deformations too.

In order to find a ligament design without plastic deformation, the ligament's width is reduced to $d = 0.25$ mm. This results in a reduced out-of-plane stiffness of the LMS, but increases anisotropy, since the LMS' in-plane compliance is more dependent on the ligaments' width than the LMS' out-of-plane stiffness. Additionally, a free-form fillet optimised for bending loads with a stress concentration factor of 1.008 under pure bending loads, designed by Waldmann et al. [57], is introduced at the ligament's ends (Fig. 16b). When subjected to $\varepsilon_y = 0.161$, the slenderness of the ligament limits the von Mises stresses to 30.5 MPa at the root and the optimised fillet effectively prevents stress concentrations.

With a strain of $\varepsilon_y = 0.4$, which includes most of the theoretical design space (cf. Section 2.3.2), the extremely localised, maximum stress is 62.5 MPa and remains below the yield stress, $\sigma_{plast} = 65.0$ MPa. Beyond that, the stresses at the beam's root are significantly lower than observed in Fig. 16a and uncritical in terms of plastification.

The ligament design depends on the application's in-plane strains. It generally holds that the higher the expected strains, the more slender the ligament should be. Additionally, the integration of a stress optimised fillet is recommended for high strain appli-

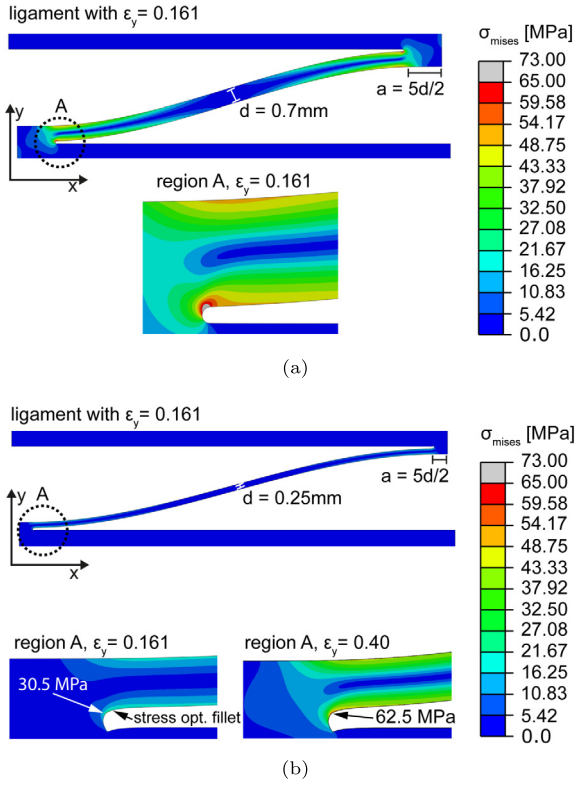

Fig. 16. Ligament stresses for the (a) standard LMS configuration (Table 1), and a more slender ligament with stress optimised fillet (b).

cations. It can be realised without additional manufacturing effort in a laser cutting process, given a laser machining system accurate enough.

6. Conclusion and outlook

This article presents the design, manufacturing and application of a three-layered morphing skin with a closed surface. The LMS can extend the application range of morphing skins beyond uniaxial strain scenarios, such as camber and span morphing, due to its bi-axial deformability and high anisotropy. The LMS is applied to a camber morphing transition region dimensioned for the size and loads of a Cessna 172 aileron. Within the transition region, the LMS undergoes bi-axial strains of 16% in chord and up to 10% in span direction and enables a trailing edge deflection of 48.7 mm over 240 mm chord length. Simulations of the LMS' out-of-plane deformation show that wing loads of 632 Pa cause less than 1.19 mm of displacement and confirm the LMS' applicability to small aircraft.

Detailed analysis quantifies the mechanical performance and anisotropy of the LMS. In practice the LMS can be designed for strains up to 40% if stress optimised, slender ligament geometries are chosen. A global poisson's ratio of 0 is provided over the whole deformation range, decoupling the morphing directions and allowing for independent bi-axial deformation of the LMS. Experiments and a validated finite element model show that the out-of-plane stiffness of the LMS is two orders of magnitude higher than an isotropic material with equivalent in-plane stiffness. The LMS' shear stiffness, tailorable via the skin's pre-strain, is at least one order of magnitude higher than the reference material.

Despite promising mechanical properties and the applicability to complex strain fields, the LMS cannot elude the highly contradicting requirements set for morphing skins and compromises on surface quality and weight. When deformed, the LMS' surface is not perfectly smooth, but the platelets cause small gaps and protrude. The surface imperfections are small, but could cause significant aerodynamic drag in laminar flow conditions. Therefore, the application of the LMS is suggested for turbulent flow regimes in the last 35% of the wing's chord where the drag penalty is less dependent on the skin's surface quality. A transition region for camber morphing control surfaces provides such flow conditions and due to its small surface area the skin's contribution to the total mass of a small aircraft is negligible, making the LMS a functional morphing skin for camber morphing transition regions. However, the aerodynamic effect of the LMS' imperfect surface and the overall aerodynamic gain of the wing system needs to be confirmed in a detailed aerodynamic study.

As the LMS design itself is material independent, changing from POM-C with its low specific stiffness to fibre reinforced polymers can be an option to further reduce skin thickness and therefore weight, while keeping the out-of-plane stiffness constant. As the LMS allows large two-dimensional strains, it is also worth to consider a multifunctional control surface instead of designated flaps and ailerons for further weight savings.

Overall, the LMS extends the application range of structural morphing skins and can replace elastomeric covers, potentially improving system performance. However, this is limited to local application and turbulent flow and should be verified in further aerodynamic studies.

Declaration of competing interest

The authors declare that they have no known competing financial interests or personal relationships that could have appeared to influence the work reported in this paper.

Data availability

The raw data required to reproduce these findings is available at https://doi.org/10.3929/ethz-b-000513115.

Acknowledgements

The research project is funded through the Swiss National Science Foundation Grant SNF 200021_192082. The Digital Image Correlation equipment was purchased through the Swiss National Science Foundation Grant SNF 206021_150729.

References

[1] S. Barbarino, O. Bilgen, R.M. Ajaj, M.I. Friswell, D.J. Inman, A review of morphing aircraft, J. Intell. Mater. Syst. Struct. 22 (9) (2011) 823–877, https://doi.org/10.1177/1045389X11414084.
[2] D.A. Burdette, J.R. Martins, Impact of morphing trailing edges on mission performance for the common research model, J. Aircr. 56 (1) (2019) 369–384, https://doi.org/10.2514/1.C034967.
[3] B.K. Woods, L. Parsons, A.B. Coles, J.H. Fincham, M.I. Friswell, Morphing elastically lofted transition for active camber control surfaces, Aerosp. Sci. Technol. 55 (2016) 439–448, https://doi.org/10.1016/j.ast.2016.06.017.
[4] U. Fasel, P. Tiso, D. Keidel, P. Ermanni, Concurrent design and flight mission optimization of morphing airborne wind energy wings, AIAA J. 59 (4) (2021) 1254–1268, https://doi.org/10.2514/1.J059621.
[5] S. Ameduri, A. Concilio, Morphing wings review: aims, challenges, and current open issues of a technology, Proc. Inst. Mech. Eng., Part C, J. Mech. Eng. Sci. (2020), https://doi.org/10.1177/0954406220944423.
[6] A. Concilio, L. Lecce, Historical background and current scenario, in: Morphing Wing Technologies: Large Commercial Aircraft and Civil Helicopters, Butterworth-Heinemann, 2018, pp. 3–84.
[7] M.T. Kikuta, Mechanical Properties of Candidate Materials for Morphing Wings, 2003.
[8] F. Previtali, A.F. Arrieta, P. Ermanni, Investigation of the optimal elastic and weight properties of passive morphing skins for camber-morphing applications, Smart Mater. Struct. 25 (5) (2016), https://doi.org/10.1088/0964-1726/25/5/055040.

[9] H. You, S. Kim, J. Yun, Design criteria for variable camber compliant wing aircraft morphing wing skin, AIAA J. 58 (2) (2020) 867–878, https://doi.org/10.2514/1.J058002.
[10] V. Ott, D. Keidel, M. Kölbl, P. Ermanni, Investigation of an adaptive, hinge-less, and highly shear stiff structure for morphing skins, J. Intell. Mater. Syst. Struct. 31 (3) (2020) 445–456, https://doi.org/10.1177/1045389X19891527.
[11] T. Yokozeki, A. Sugiura, Y. Hirano, Development of variable camber morphing airfoil using corrugated structure, J. Aircr. 51 (3) (2014) 1023–1029, https://doi.org/10.2514/1.C032573.
[12] F. Previtali, A.F. Arrieta, P. Ermanni, Performance of a three-dimensional morphing wing and comparison with a conventional wing, AIAA J. 52 (2014) 2101–2113, https://doi.org/10.2514/1.J052764.
[13] D. Keidel, G. Molinari, P. Ermanni, Aero-structural optimization and analysis of a camber-morphing flying wing: structural and wind tunnel testing, J. Intell. Mater. Syst. Struct. 30 (6) (2019) 908–923, https://doi.org/10.1177/1045389X19828501.
[14] F. Previtali, G. Molinari, A.F. Arrieta, M. Guillaume, P. Ermanni, Design and experimental characterisation of a morphing wing with enhanced corrugated skin, J. Intell. Mater. Syst. Struct. 27 (2) (2016) 278–292, https://doi.org/10.1177/1045389X15595296.
[15] R. Navaratne, I. Dayyani, B.K.S. Woods, M.I. Friswell, Development and testing of a corrugated skin for a camber morphing aerofoil, in: AIAA SciTech Forum, January 2015, pp. 1–10.
[16] M. Kölbl, M. Sakovsky, P. Ermanni, A highly anisotropic morphing skin unit cell with variable stiffness ligaments, Compos. Struct. 254 (2020) 112801, https://doi.org/10.1016/j.compstruct.2020.112801.
[17] J. Sun, L. Du, F. Scarpa, Y. Liu, J. Leng, Morphing wingtip structure based on active inflatable honeycomb and shape memory polymer composite skin: a conceptual work, Aerosp. Sci. Technol. 111 (2021) 106541, https://doi.org/10.1016/j.ast.2021.106541.
[18] A. Vigliotti, D. Pasini, Analysis and design of lattice materials for large cord and curvature variations in skin panels for morphing wings, Smart Mater. Struct. 24 (3) (2015) 037006, https://doi.org/10.1088/0964-1726/24/3/037006.
[19] K. Olympio, F. Gandhi, Zero-v cellular honeycomb flexible skins for one-dimensional wing morphing, in: 48th AIAA/ASME/ASCE/AHS/ASC Structures, Structural Dynamics, and Materials Conference, April 2007, pp. 1–28.
[20] K.R. Olympio, F. Gandhi, Flexible skins for morphing aircraft using cellular honeycomb cores, J. Intell. Mater. Syst. Struct. 21 (17) (2010) 1719–1735, https://doi.org/10.1177/1045389X09350331.
[21] K.R. Olympio, F. Gandhi, Zero poisson's ratio cellular honeycombs for flex skins undergoing one-dimensional morphing, J. Intell. Mater. Syst. Struct. 21 (17) (2010) 1737–1753, https://doi.org/10.1177/1045389X09355664.
[22] J. Huang, Q. Zhang, F. Scarpa, Y. Liu, J. Leng, Bending and benchmark of zero Poisson's ratio cellular structures, Compos. Struct. 152 (2016) 729–736, https://doi.org/10.1016/j.compstruct.2016.05.078.
[23] J. Huang, Q. Zhang, F. Scarpa, Y. Liu, J. Leng, In-plane elasticity of a novel auxetic honeycomb design, Composites Part B: Engineering 110 (2017) 72–82, https://doi.org/10.1016/j.compositesb.2016.11.011.
[24] R.M. Ajaj, C.S. Beaverstock, M.I. Friswell, Morphing aircraft: the need for a new design philosophy, Aerosp. Sci. Technol. 49 (2016) 154–166, https://doi.org/10.1177/1045389X13502869.
[25] S. Vasista, L. Tong, K.C. Wong, Realization of morphing wings: a multidisciplinary challenge, J. Aircr. 49 (1) (2012) 11–28, https://doi.org/10.2514/1.C031060.
[26] G.A. Lesieutre, J.A. Browne, M.I. Frecker, Scaling of performance, weight, and actuation of a 2-D compliant cellular frame structure for a morphing wing, J. Intell. Mater. Syst. Struct. 22 (10) (2011) 979–986, https://doi.org/10.1177/1045389X11412641.
[27] W.A. Klimczyk, Z.J. Goraj, Analysis and optimization of morphing wing aerodynamics, Aircr. Eng. Aerosp. Technol. 91 (3) (2019) 538–546, https://doi.org/10.1108/AEAT-12-2017-0289.
[28] A.M. Pankonien, J.O. Hardin, N. Bhagat, G.W. Reich, J.D. Berrigan, From model to manufacture: additive aeroelastic morphing testbeds, in: International Forum on Aeroelasticity and Structural Dynamics IFASD, 2017.
[29] E. Hearn, Strain energy, in: Mechanics of Materials 1, Elsevier, 1997, pp. 254–296.
[30] J. McIver, Cessna Skyhawk II/100 Performance Assessment, Tech. Rep., Temporal Images (Admiral Valley Pty Ltd.), AU-Ormond 3204, 2003.
[31] M.H. Sadraey, Aircraft Design: A Systems Engineering Approach, John Wiley & Sons, 2012.
[32] Federal Aviation Administration, Type certificate data sheet No. 3A12, Tech. Rep., Federal Aviation Administration, Washington DC, US, 2019.
[33] J. Johansen, J.N. Sørensen, Prediction of laminar/turbulent transition in airfoil flows, J. Aircr. 36 (4) (1999) 731–734, https://doi.org/10.2514/2.2501.
[34] Cessna Aircraft Company, Pilot's Operating Handbook Skyhawk CESSNA MODEL 172N, Tech. Rep., Cessna Aircraft Company, Wichita US-KS, 1977.
[35] B.K.S. Woods, M.I. Friswell, Structural analysis of the fish bone active camber concept, in: Italian Association of Aeronautics and Astronautics XXII Conference, 2013.
[36] B.K. Woods, O. Bilgen, M.I. Friswell, Wind tunnel testing of the fish bone active camber morphing concept, J. Intell. Mater. Syst. Struct. 25 (7) (2014) 772–785, https://doi.org/10.1177/1045389X14521700.
[37] A.E. Rivero, P.M. Weaver, J.E. Cooper, B.K. Woods, Parametric structural modelling of fish bone active camber morphing aerofoils, J. Intell. Mater. Syst. Struct. 29 (9) (2018) 2008–2026, https://doi.org/10.1177/1045389X18758182.
[38] A.E. Rivero, S. Fournier, M. Manolesos, J.E. Cooper, B.K. Woods, Wind tunnel comparison of flapped and fishbac camber variation for lift control, in: AIAA Scitech 2020 Forum, Vol. 1 Part F, 2020, pp. 1–18.
[39] C. Thill, J.D. Downsborough, S.J. Lai, I.P. Bond, D.P. Jones, Aerodynamic study of corrugated skins for morphing wing applications, Aeronaut. J. 114 (1154) (2010) 237–244.
[40] E.N. Jacobs, Report no. 446 airfoil section characteristics as affected by protuberances, in: Nineteenth Annual Report of the National Advisory Committee for Aeronautics, 1933, pp. 109–124.
[41] F. Mishriky, P. Walsh, Effect of the backward-facing step location on the aerodynamics of a morphing wing, Aerospace 3 (4) (2016) 25, https://doi.org/10.3390/aerospace3030025.
[42] P.R. Childs, Seals, in: Mechanical Design Engineering Handbook, Elsevier, 2019, pp. 657–717.
[43] B. Hodkinson, Estimation of the leakage through a labyrinth gland, Proc. Inst. Mech. Eng. 141 (1) (1939) 283–288, https://doi.org/10.1243/pime_proc_1939_141_037_02.
[44] H. Zimmermann, K.H. Wolff, Air system correlations part 1: labyrinth seals, in: ASME 1998 International Gas Turbine and Aeroengine Congress and Exhibition, 1998.
[45] E.N. Peters, Engineering termoplastics-materials, properties, trends, in: Applied Plastics Engineering Handbook: Processing, Materials, and Applications, second edition, Elsevier Inc., 2017, pp. 3–26.
[46] S. Lüftl, P.M. Visakh, S. Chandran, Polyoxymethylene Handbook, John Wiley & Sons, Inc., Hoboken, NJ, USA, 2014.
[47] Y. Rémond, M. Védrines, Measurement of local elastic properties of injection moulded polymer structures by analysis of flexural resonant frequencies. Applications in POM, PA66, filled PA 66, Polym. Test. 23 (3) (2004) 267–274, https://doi.org/10.1016/j.polymertesting.2003.08.005.
[48] Z. Károly, G. Kalácska, L. Zsidai, M. Mohai, S. Klébert, Improvement of adhesion properties of polyamide 6 and polyoxymethylene-copolymer by atmospheric cold plasma treatment, Polymers 10 (12) (2018) 1380, https://doi.org/10.3390/polym10121380.
[49] ISO 527-1:2019, Plastics – determination of tensile properties – Part 1: General principles, Tech. Rep., International Organization for Standardization, Geneva, CH, 2019.
[50] G.L. Farley, D.J. Baker, In-plane shear test of thin panels, Exp. Mech. 23 (1) (1983) 81–88.
[51] S. Lee, M. Munro, Evaluation of in-plane shear test methods for advanced composite materials by the decision analysis technique, Composites 17 (1) (1986) 13–22, https://doi.org/10.1016/0010-4361(86)90729-9.
[52] B. Černe, R. Lorber, J. Duhovnik, J. Tavčar, Influence of temperature- and strain rate-dependent viscoplastic properties of polyoxymethylene on the thermo-mechanical response of a steel-polyoxymethylene spur gear pair, Mater. Today Commun. 25 (2020) 101078, https://doi.org/10.1016/j.mtcomm.2020.101078.
[53] Kundert AG, Werkstoff-Datenblat POM C natur, 2021.
[54] Ensinger GmbH, TECAFORM AH natural - Stock Shapes (rods, plates, tubes), 2020.
[55] H. Shercliff, M. Ashby, Elastic structures in design, in: Reference Module in Materials Science and Materials Engineering, Elsevier, 2016.
[56] S.P. Timoshenko, S. Woinowsky-Krieger, Theory of Plates and Shells, 2nd edition, McGraw-Hill, New York, 1964.
[57] W. Waldman, M. Heller, G.X. Chen, Optimal free-form shapes for shoulder fillets in flat plates under tension and bending, Int. J. Fatigue 23 (6) (2001) 509–523, https://doi.org/10.1016/S0142-1123(01)00011-1.